Toward a live homogeneous database of solar active regions based on SOHO/MDI and SDO/HMI synoptic magnetograms. II. parameters for solar cycle variability

Ruihui Wang,[1,2] Jie Jiang,[1,2] and Yukun Luo[1,2]

[1] *School of Space and Environment, Beihang University, Beijing, People's Republic of China; jiejiang@buaa.edu.cn*
[2] *Key Laboratory of Space Environment Monitoring and Information Processing of MIIT, Beijing, People's Republic of China*

ABSTRACT

Solar active regions (ARs) determine solar polar fields and cause solar cycle variability within the framework of the Babcock-Leighton (BL) dynamo. The contribution of an AR to the polar field is measured by its dipole field, which results from flux emergence and subsequent flux transport over the solar surface. The dipole fields contributed by an AR before and after the flux transport are referred to as the initial and final dipole fields, respectively. For a better understanding and prediction of solar cycles, in this paper, we provide a database including AR's initial and final dipole fields and the corresponding results of their bipolar magnetic region (BMR) approximation from 1996 onwards. We also identify the repeated ARs and provide the optimized transport parameters. Based on our database, we find that although the commonly used BMR approximation performs well for the initial dipole field, it exhibits a significant deviation for the final dipole field. To accurately assess an AR's contribution to the polar field, the final dipole field with its real configuration should be applied. Despite the notable contributions of a few rogue ARs, approximately the top 500 ARs ordered by their final dipole fields are necessary to derive the polar field at the cycle minimum. While flux transport may increase or decrease the dipole field for an individual AR, its collective impact over all ARs in a cycle is a reduction in their total dipole field.

1. INTRODUCTION

Solar active regions (ARs) are common features on the solar surface (van Driel-Gesztelyi & Green 2015), originating from the emergence of flux tubes (Fan 2009; Cheung et al. 2010). They determine solar polar fields and cause the solar cycle variability. In the Babcock-Leighton (BL) dynamo, the emergence of ARs and the subsequent transport of erupted AR flux on the surface reverse the existing poloidal field, generating a new poloidal field with the opposite polarity (Babcock 1961; Leighton 1964). This poloidal field is then stretched by differential rotation, giving rise to the toroidal field, which influences the strength of the subsequent solar cycle. Therefore, a correlation between the poloidal field, or polar field, during solar minimum and the strength of the subsequent cycle is expected, and observations con-

firm the linear correlation between them (Schatten et al. 1978; Jiang et al. 2007; Muñoz-Jaramillo et al. 2013). If the contribution of all ARs in a given cycle is known, we can predict the polar field in solar minimum, and the strength of the following cycle. Such predictions are crucial for forecasting the frequency and intensity of future solar activities, as well as for planning future space missions (Jiang et al. 2018; Petrovay 2020).

The contribution of an AR to the polar field can be quantified by its axial dipole field, also known as the axial dipole moment. The axial dipole field of an AR originates from flux emergence and changes due to flux transport across the solar surface (Wang & Sheeley 1991). The dipole field of an AR immediately after its emergence is termed the initial dipole field (D_i). The initial dipole field is primarily influenced by the latitude difference between the two polarities of ARs, described by the polarity separation and tilt angle when optimized to a bipolar magnetic region (BMR).

However, D_i only describes the contribution of flux emergence. Subsequent to emergence, AR dipole fields

Corresponding author: Jie Jiang
jiejiang@buaa.edu.cn

increase or decrease during flux transport (Wang & Sheeley 1991; Jiang et al. 2014a). The dipole field after flux transport is referred to as the final dipole field (D_f). During flux transport, a portion of the AR flux diffuses across the equator due to supergranular diffusion and is then transported to the pole via meridional flow and supergranular diffusion (Jiang et al. 2014b; Wang 2017; Yeates et al. 2023). Simultaneously, an equivalent amount of net flux with the opposite polarity to the cross-equatorial flux is transported to the other pole. The cross-equatorial flux dictates the final flux distribution of ARs and, consequently, determines D_f (Cameron et al. 2013; Petrovay et al. 2020). An AR's latitude and transport parameters, which include supergranular diffusivity and meridional flow velocity, influence the cross-equatorial flux, leading to the variation in D_f.

For ARs emerging near the solar equator, the absolute values of their D_i are dramatically increased by flux transport. Given that these ARs may not strictly obey Hale's law and Joy's law, they can significantly increase or decrease the polar field and the strength of the following cycle. Those ARs are regarded as rogue ARs. Jiang et al. (2015) demonstrated that the weak cycle 24 is related to several rogue ARs in cycle 23. Moreover, Nagy et al. (2017) found that some rogue ARs have the potential to halt the dynamo, leading to a grand minimum. The contribution of rogue ARs can only be accurately assessed through D_f.

ARs are usually approximated as symmetric bipolar magnetic regions (BMRs) in studies concerning their emergence and evolution. However, the actual configuration of an AR is complex and often deviates significantly from a BMR. Firstly, the two polarities of an AR are commonly asymmetric in terms of both flux and area (van Driel-Gesztelyi & Petrovay 1990; Tlatov et al. 2014). This asymmetry can substantially reduce or even reverse the dipole field of an AR compared to a symmetric one (Iijima et al. 2019; Wang et al. 2021). Secondly, there are many ARs with complex configurations, such as δ-type ARs. The dipole fields of these ARs sometimes change their sign during flux transport (Jiang et al. 2019), which can not be described by symmetric BMRs. Yeates (2020) demonstrated that the BMR approximation tends to overestimate the solar axial dipole field during the minimum compared to real ARs. Including the real configuration of ARs, Wang et al. (2021) proposed a general method that calculates D_f of ARs more accurately than the method based on BMR approximation. They both emphasize the significance of considering the real configuration of ARs in obtaining their D_f.

The initial dipole field, D_i, specifically characterizes the contribution of flux emergence to the polar field, while D_f encompasses both the contributions of flux emergence and flux transport. When considering the limitations of BMR approximation, the real contribution of an AR to the polar field can only be accurately measured by its D_f while taking into account its real configuration. As flux transport can either increase or decrease the dipole fields of individual ARs, a key question arises: what is the overall impact of flux transport on all ARs in a solar cycle? Wang & Sheeley (1991) shows that the overall effect of flux transport over a solar cycle is a decrease in the dipole field originating from flux emergence. Their study only includes ARs in cycle 21, necessitating further research.

A database providing both D_i and D_f contributes to investigating the roles of flux emergence and flux transport in the BL mechanism. Moreover, such a database can serve as a valuable resource for studying the influence of ARs, particularly rogue ones, on the polar field and solar cycle variability, known as dynamo effectivity (Petrovay et al. 2020), and subsequently aid in predicting solar cycles.

However, most existing AR databases only provide basic parameters and parameters related to space weather (Wang & Sheeley 1989; Bobra et al. 2014, 2021; Muñoz-Jaramillo et al. 2021; Sreedevi et al. 2023). An exception is the work by Yeates (2020), which provides a database containing D_i and D_f for cycle 24 based on SHARPs data (Bobra et al. 2014). Here, we aim to construct a live, comprehensive, and homogeneous AR database covering cycles 23, 24, and 25 in a series of papers. This database will encompass two sets of parameters: the first set includes fundamental AR parameters like number, area, and flux, while the second set includes parameters directly for solar cycle variability, such as D_i, D_f, and their BMR approximations, D_i^B and D_f^B. In the first paper of the series (Wang et al. 2023), we develop an automated AR detection method based on SOHO/MDI and SDO/HMI synoptic magnetograms (Scherrer et al. 1995, 2012). We then provide the first set of parameters based on these detections. In this paper, we first address the issue of repeated ARs in the detections and then present the second set of parameters. Based on a substantial number of AR observations in our database, we systematically explore the disparities between D_i and D_f and show the impact of flux transport and flux emergence on the dipole field. Furthermore, we analyze the effects of BMR approximation, as well as the influence of a few rogue ARs and numerous ARs with small D_f.

This paper is organized as follows. In Section 2, we identify and remove repeat ARs. In Section 3, we opti-

mize the transport parameters and calculate the D_i, D_f, and their BMR approximations. In Section 4, we compare D_i and D_f of real ARs, show the impact of BMR approximation on D_i and D_f, and analyze the impact of many ARs with small D_f on the cumulative final dipole field. In Section 5, we summarize and discuss the above results.

2. IDENTIFICATION AND REMOVAL OF REPEAT ACTIVE REGIONS

Some ARs with strong fluxes can live for many Carrington rotations (CRs) (Harvey 1993; Li & Welsch 2008). Their impacts on the end-of-cycle polar field are usually significant. The removal of these repeated observations is crucial for an accurate reconstruction of the polar field. In the first paper of the series, Wang et al. (2023), we have developed an AR automatic detection method, which consists of five modules. The first module employs adaptive intensity threshold segmentation, while the second module incorporates morphological closing and opening operations. These modules jointly eliminate background magnetic fields and decayed ARs and extract kernel pixels of ARs. The third module, region growing, utilizes these kernel pixels as seeds to recover all pixels associated with each AR. Modules 4 and 5 work together to eliminate decayed ARs that persist even after the region-growing process. The fourth module involves a morphological closing operation and a small-region removal operation. The fifth module consists of a morphological dilation operation for merging neighboring regions and a unipolar region removal operation based on their flux imbalance.

The aforementioned detection method processes each synoptic magnetogram independently and thus can not identify repeated ARs. To address this limitation, we introduce a repeat-AR-removal module positioned between Module 4 and Module 5. Adding this module before Module 5 aims to avoid the potential impact of merging neighbor regions in Module 5, enhancing the method's ability to identify and remove repeated ARs. The step-by-step procedures of the repeat-AR-removal module are visually presented in Figure 1, with the CR 1968 map serving as an example.

In the process of removing repeat ARs in the CR 1968 map, we also utilize the synoptic magnetogram from the last CR, 1967. After Module 4, the AR detection algorithm has identified all potential ARs and eliminated small, decayed AR segments. Subsequently, we derotate the detected ARs to the last CR to compensate for the effects of differential rotation. Then we obtain masks. Each mask of an AR, depicted by orange lines in panel (b), labels the region where the flux of the AR in CR
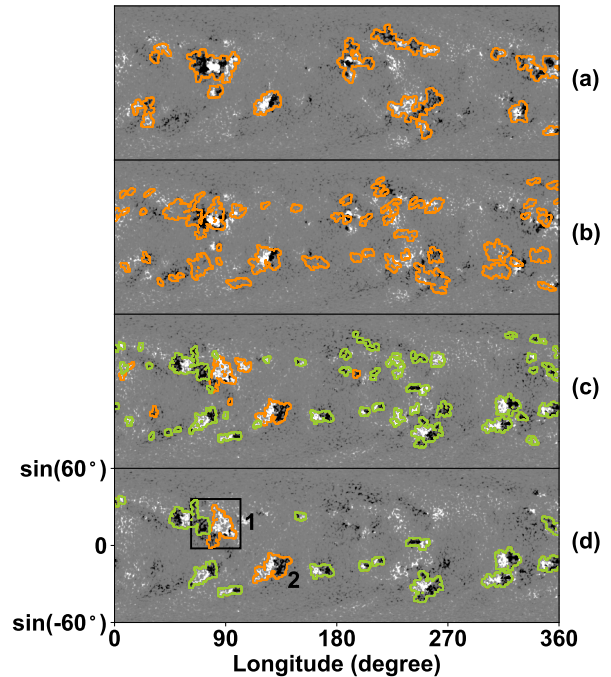

Figure 1. Illustration of the repeat-AR-removal module, using the synoptic magnetogram of CR 1968 as an example. Panel (a) is the map of CR 1967, with the AR detection result outlined in orange lines. Panel (b) is the map of CR 1967, overplotted with the masks of ARs detected in CR 1968. Panel (c) is the AR detection result of CR 1968 after the repeat-AR-removal module, and panel (d) is the final detection result after module 5. In panels (c) and (d), the repeat ARs are labeled with orange lines, and new ARs are labeled with green lines. In panel (d), two detected repeat ARs are labeled with No. 1 and 2. The black square labels the corresponding result, estimated by the naked eye, of the repeat AR No.1.

1968 comes. We apply the differential rotation profile

$$\omega(\lambda) = \omega_a + \omega_b sin^2(\lambda) + \omega_c sin^4(\lambda), \qquad (1)$$

where λ is the latitude. $\omega_a = 0.362°day^{-1}$, $\omega_b = -2.040°day^{-1}$, and $\omega_c = -1.487°day^{-1}$. These values are provided by the header file of the MDI and HMI synoptic magnetograms.

Then we conduct a comparison between the unsigned flux in CR 1968 (F_n^{us}, where n denotes the n-th map, i.e., CR 1968 map) and the unsigned flux of the CR 1967 map within the mask (F_{n-1}^{us}, where n-1 denotes the n-1-th map, i.e., CR 1967 map) for each detected AR in CR 1968. If the ratio F_{n-1}^{us}/F_n^{us} exceeds a defined threshold (T_{fr}) and the AR satisfies the polarity condition, we regard the AR as a repeat observation of an AR in CR 1967. Considering the impact of other flows on the solar surface, such as the meridional flow and supergranulation, the mask obtained by derotating

an AR to the last CR may not precisely represent the true area where the flux of the AR originates. Therefore, the threshold doesn't necessarily have to be set to 1, and after experiments, we set $T_{fr} = 0.7$ for optimal results. The polarity condition is

$$\left| \frac{F_n}{F_n^{us}} \frac{F_{n-1}}{F_{n-1}^{us}} \right| sign(\frac{F_n}{F_{n-1}}) > -0.5, \qquad (2)$$

where F_n, F_{n-1} are the net flux of AR in CR 1968 and the net flux of CR 1967 map within the mask, respectively. The term $sign(\frac{F_n}{F_{n-1}})$ is utilized to determine whether the sign of the AR net flux in two maps is the same. The ratios $\frac{F_n}{F_n^{us}}$ and $\frac{F_{n-1}}{F_{n-1}^{us}}$ are employed to assess the flux imbalance of AR in CR 1968 map and AR in CR 1967 map, respectively. This condition prevents the unipolar regions, which differ in polarity from the unipolar regions in the last map, from being wrongly identified as repeat regions. The result is shown in panel (c), where the region labeled in the orange line represents repeat ARs that have been successfully detected and removed. Finally, we apply Module 5 to merge neighbor regions and remove unipolar regions. The final detection result of CR 1968 is shown in panel (d).

The repeat-AR-removal module successfully removes two repeat ARs in the MDI map of CR 1968, labeled with No. 1 and 2. A visual comparison between panels (d) and (a) reveals that AR No. 2 is a clear repeat observation of a former AR. However, the situation for AR No. 1 is more complex. It constitutes only a portion of the entire AR, where a new AR emerges near the former one. Such ARs are commonly referred to as activity complexes (ACs) (Harvey 1993; Gaizauskas et al. 1983; Wang et al. 2020). Comparing the two maps in CRs 1967 and 1968 with the naked eye, we can find that the repeat regions in the AC should be regions within the black square. While the actual repeat region might be slightly larger than the region we detected, the module still identifies the repeat AR within the AC. The results of the CR 1968 map demonstrate that our repeat-AR-removal module is not only capable of removing obvious repeat ARs but can also address cases of repeat decayed ARs within ACs. It's worth noting that, at times, the module may face challenges in accurately detecting repeat regions due to the segmentation of single ARs in modules 1-4 of Wang et al. (2023).

After removing repeat ARs, the total number of detected ARs decreases from 2579 to 2495 over two solar cycles. Specifically, the number of ARs in cycles 23 and 24 reduces from 1481 to 1436 and from 1098 to 1059, respectively. Yeates (2020) detects 143 repeat ARs during cycle 24, a higher count compared to our detection result of 39 repeat ARs. Discrepancies in the number of

repeat ARs could be attributed to the use of a smaller threshold, $T_{fr} = 0.7$, in our detection in contrast to the threshold $T_{fr} = 1$ employed by Yeates (2020). Additionally, discrepancies may also arise from the fact that some repeat ARs in our results are just part of the whole AC and do not affect the AR number.

3. CALCULATION OF DIPOLE FIELDS
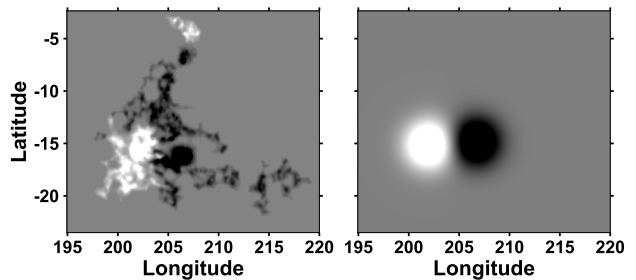
3.1. Calculation methods of dipole fields

Figure 2. Illustration of an AR (left panel) and its corresponding BMR approximation (right panel). The AR is detected in the MDI synoptic magnetogram of CR 1961, with label No. 6 in our database. Its NOAA number is 08936.

After removing repeat ARs in our database, we calculate the axial dipole fields of ARs, including the initial dipole field (D_i) and final dipole field (D_f). Each parameter is determined using two distinct methods: one based on the actual configuration of ARs, termed the AR method, and the other based on the BMR approximation, referred to as the BMR method. For the BMR approximation, we approximate each polarity of AR as a finite-sized Gaussian-like polarity patch (van Ballegooijen et al. 1998; Jiang et al. 2014b). Figure 2 shows an example of an AR and its BMR approximation.

The axial dipole field of an AR is the coefficient of the Y_1^0 term in the spherical harmonic expansion of its radial magnetic fields. Mathematically, this is expressed as:

$$D_i = \frac{3}{4\pi} \iint B(\lambda, \varphi) sin\lambda cos\lambda d\lambda d\varphi, \qquad (3)$$

where λ and φ denote latitude and longitude, respectively, and $B(\lambda, \varphi)$ is the radial magnetic field distribution of the AR. When applying the BMR approximation to an AR, Equation (3) can be simplified as:

$$D_i^B = \frac{3}{4\pi R_\odot^2} \Phi d_\lambda cos\lambda, \qquad (4)$$

where Φ represents the unsigned flux of one polarity of the BMR. d_λ is the latitude difference of the BMR. It can be calculated using the latitude of the positive

polarity minus the latitude of the negative polarity, or as $d_\lambda = d \sin \alpha$, where d is the polarity separation, and α is the tilt angle (Wang & Sheeley 1991; Yeates et al. 2023).

Equations (3) and (4) are used to quantify the axial dipole field of an AR when it emerges on the solar surface, referred to as the initial dipole field (D_i). After a BMR emergence, its axial dipole field changes due to meridional flow and supergranular diffusion. The ratio (f_∞) between the dipole field at the end of a BMR's evolution (final dipole field, D_f) and D_i follows a Gaussian relation about the BMR emergence latitude λ_0. The relation is expressed as $f_\infty \propto \exp(-a\lambda_0^2)$, where a is a constant (Jiang et al. 2014a). Petrovay et al. (2020) provide an algebraic expression for f_∞, and thus provide an algebraic method to calculate the final dipole field of a BMR (D_f^B). The method is

$$D_f^B = f_\infty D_i^B, \quad (5)$$

where f_∞ is given by

$$f_\infty = \frac{a}{\lambda_R^B} exp\left(-\frac{\lambda_0^2}{2(\lambda_R^B)^2}\right), a = \frac{n+1}{n+2}\sqrt{\frac{2}{\pi}}. \quad (6)$$

In Equation (6), λ_0 represents the emergence latitude of the BMR, and n describes the approximated polar field profile in solar minimum, i.e. $B(\lambda) \propto \sin^n(\lambda)$. The value of n is set to 7 in our calculations, following the value of Wang et al. (2009). λ_R^B is the dynamo effectivity range, calculated by:

$$\lambda_R^B = \sqrt{\frac{\eta}{R_\odot^2 \Delta u} + \sigma_0^2}. \quad (7)$$

Here, η is the supergranular diffusivity, Δu is the divergence of the meridional flow at the equator, i.e., $\frac{1}{R_\odot}\frac{du}{d\lambda}\big|_{\lambda=0}$, and σ_0 is the initial Gaussian width of the BMR.

However, Equation (5) just applies to BMRs. For ARs with arbitrary configurations, Wang et al. (2021) provides a more general method expressed as

$$D_f = A_0 \iint B(\lambda, \varphi) erf(\frac{\lambda}{\sqrt{2}\lambda_R}) cos\lambda d\lambda d\varphi, \quad (8)$$

where A_0 is a constant, set to 0.21 according to Wang et al. (2021). In this equation, the dynamo effectivity range λ_R is defined as

$$\lambda_R = \sqrt{\frac{\eta}{R_\odot^2 \Delta u}}. \quad (9)$$

This is different from λ_R^B in Equation (6), for the BMR method. The form of Equation (8) has been slightly adjusted from that presented in Wang et al. (2021) to improve its conciseness and clarity.
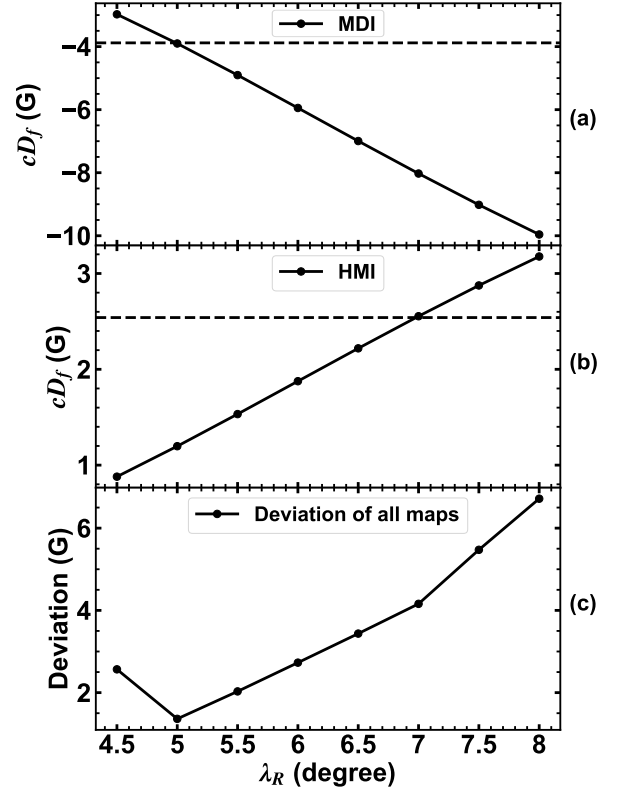

Figure 3. Comparison between cumulative final dipole fields (cD_f) for different transport parameters (λ_R) and dipole field observations of MDI maps (CRs 1909-2096) and HMI maps (CRs 2097-2225). Panels (a) and (b) depict the results of MDI and HMI maps, respectively. Black dots represent the calculated cD_f, and dashed lines show dipole field observations. Panel (c) illustrates the total deviation between cD_f and dipole field observations across all synoptic magnetograms.

3.2. Optimization of the transport parameter λ_R

In the computation of final dipole fields (D_f), the term $\frac{\eta}{R_\odot^2 \Delta u}$ is present in both the BMR method and the AR method. The meridional flow (u) and supergranular diffusivity (η) are less constrained by observations (Petrovay et al. 2020; Jiang et al. 2023). A comprehensive discussion on the observations of Δu and η is provided in Jiang et al. (2023). Δu and η are sometimes optimized with magnetogram observations when employed in Surface Flux Transport (SFT) models (Lemerle et al. 2015; Whitbread et al. 2017). According to the BL mechanism, the solar axial dipole field is built up through the emergence and evolution of ARs (Babcock 1961; Leighton 1964). Consequently, the cumulative final dipole fields (cD_f) in one solar cycle, defined as the sum of all ARs' D_f, should be equal to the difference between the axial dipole fields at the end-of-cycle solar minimum and that at the start-of-cycle mini-

mum. Since the AR method is considered more accurate than the BMR method for ARs with real configurations (Wang et al. 2021), we utilize the D_f calculated by the AR method to optimize λ_R, which is equivalent to optimizing $\frac{\eta}{R_\odot^2 \Delta u}$. We also refer to λ_R as the transport parameter.

We conduct a comparison between the cD_f and the solar dipole fields obtained from the MDI and HMI synoptic magnetograms. The MDI maps cover the time range from CR 1909 to CR 2096, roughly corresponding to cycle 23, while the HMI maps cover the time range from CR 2097 to CR 2225, roughly corresponding to cycle 24. To calculate the solar dipole field, we use the synoptic magnetograms with the polar field corrected. The correction is performed by interpolation using relatively well-observed data during September/March for many years (Sun et al. 2011; Sun 2018; Luo et al. 2023). The dipole field for the beginning or the end of a cycle is determined by averaging the dipole fields calculated in six CRs near this time.

The comparison is depicted in Figure 3. As λ_R increases, the absolute values of cD_f for both the MDI and HMI maps also increase. The optimal value of λ_R for the MDI maps is $5°$, while for the HMI maps, it is $7°$. The transport parameter λ_R used in the SFT simulation based on HMI observations by Yeates (2020) is $6.35°$, which is only slightly smaller than the parameter we use. The minor discrepancy may be attributed to the differences in the magnetic field distributions of ARs in our database and that of Yeates (2020).

To minimize the overall deviation between the cD_f and the solar dipole fields obtained from both the MDI and HMI maps, the optimal λ_R is also $5°$. This value is not the smallest among the transport parameters used in past research, such as $4°$ in Lemerle et al. (2015) and $4.36°$ in Wang (2017). The total deviation for the optimal λ_R is still significant. Factors contributing to this deviation may include the detection of new ARs in the ACs, limitations in synoptic magnetogram observations, and limitations in polar field observations. Although our detection method, incorporating the repeat-AR-removal module, can eliminate some repeated regions and detect new ARs in the ACs, it may still miss some repeat regions or erroneously remove newly emerged flux. Synoptic magnetograms lack observations of the far-side solar disk and have relatively low time resolution. The limitations in synoptic magnetogram observations may result in not all detected ARs being in their fully emerged phase, leading to the potential loss of some emerged AR flux. Additionally, synoptic maps fail to capture some short-lived ARs, particularly those emerging on the far-side of the sun. Considering the small tilt angle of the

Sun's rotation axis relative to the ecliptic and the projection effect of magnetic field observations, measurements of the polar magnetic field are poor. Magnetic field observations near polar regions often exhibit a high noise level and contain missing values. Interpolation is applied to obtain missing data (Sun et al. 2011; Luo et al. 2023), thereby affecting the polar field. As a result, the solar dipole field from the synoptic maps may also deviate from the actual value.

We use $\lambda_R = 5°$ to calculate D_f, and meanwhile, we compare the results of D_f calculated with $\lambda_R = 7°$ to show the impact of λ_R. In addition, we also provide the processing programs along with the database and anyone can calculate the parameter D_f with another λ_R if necessary.

3.3. *Calculation of dipole fields based on the detected ARs*

With the optimal transport parameter, $\lambda_R = 5°$, we apply the calculation methods described in Section 3.1 to AR detection results to calculate dipole fields for each AR. First, we balance the magnetic flux of each AR by increasing the flux of the weak polarity because a part of the flux of the more dispersed polarity, usually the following polarity, is missed by the detection. The method is the same as Wang et al. (2020) and Jiang et al. (2019). Then, we get the magnetic field distribution, $B(sin\lambda, \varphi)$, used for the AR method, directly from AR detection of the maps. Flux Φ, latitude difference d_λ, and initial Gaussian width σ_0 used in the BMR method are also calculated from the AR detection results.

To align with the results from MDI maps, the AR flux detected in HMI synoptic magnetograms needs to be multiplied by a factor of 1.36 (Wang et al. 2023). Since equations of both AR and BMR methods are linear in terms of magnetic fields, we also calibrate the AR dipole fields in HMI maps by applying a factor of 1.36. Comparing the parameters of the same AR detected in MDI and HMI maps during the overlap period, as shown in Figure 4, the factor works well for all parameters.

4. STATISTICAL PROPERTIES OF DIPOLE FIELDS

After removing repeat ARs in our detection and calculating dipole fields, we update the detected ARs in our database and provide the second set of parameters. There are 2892 ARs in our database now, from CR 1909 to CR 2278 (1996.5 - 2023.11). The second set of parameters includes the initial dipole field (D_i), the final dipole field (D_f), and the BMR approximation of the two parameters, D_i^B and D_f^B. Together with the first set of parameters, i.e. AR basic parameters, such as
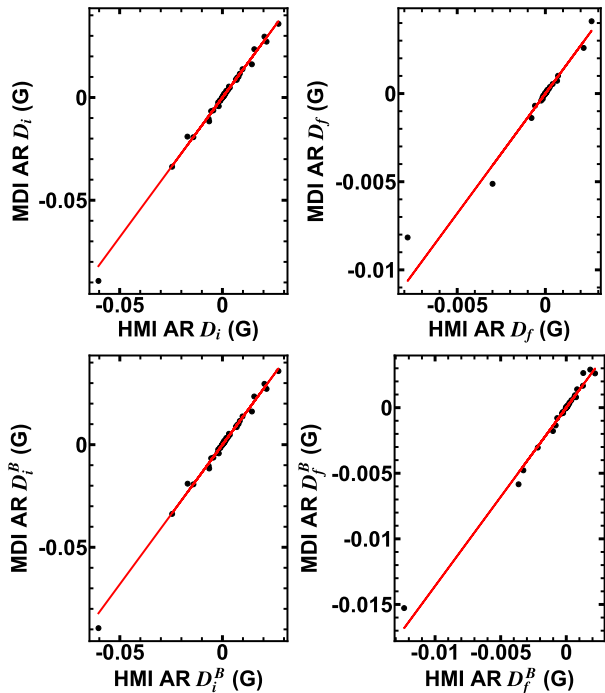
Figure 4. Calibration of AR initial dipole fields (D_i, D_i^B) and final dipole fields (D_f, D_f^B) from MDI and HMI synoptic magnetograms. The red line in each panel indicates the calibration based on AR flux, with a slope of 1.36.

location, area, and flux, our database can now provide 17 parameters. The second set of parameters can describe the contribution of ARs to the solar polar field and contribute to the understanding and prediction of solar cycles. To show the properties of the second set of parameters, we compare the D_i and D_f, analyze the impact of BMR approximation on the dipole fields, and investigate the impact of ARs with small D_f on the cumulative final dipole fields.

4.1. *Difference between D_i and D_f*

First, we systematically compare the initial dipole field (D_i) and final dipole field (D_f) of ARs with real configurations to illustrate the impact of flux transport on each AR and all ARs in a solar cycle. Figure 5 shows the distribution of D_i and D_f. Both D_i and D_f exhibit concentration around zero, with the distribution of D_f being more centered than D_i. D_i tends to be negative during cycle 23 and positive in cycle 24, while D_f shows a more symmetric distribution around zero for both cycles. Although some ARs exhibit significant D_i and D_f, the majority have relatively small D_i or D_f. In two cycles, 1709 ARs, approximately 68% of all ARs, have an absolute D_i smaller than 0.01 G, which is less than 1% of the total dipole field. The corresponding number for D_f is 2002, accounting for about 80%. While certain ARs

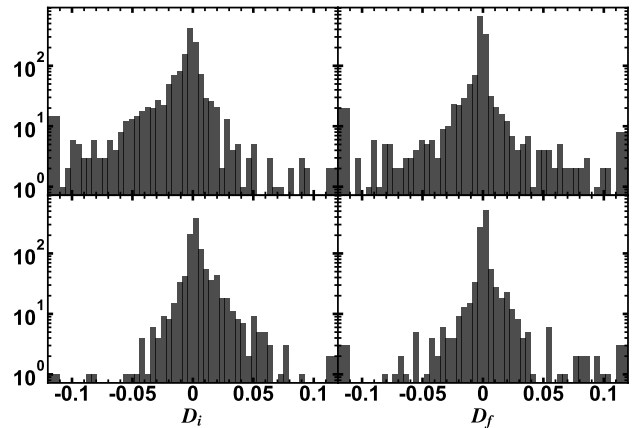can notably influence the solar dipole field, the impact of most ARs is limited.

Figure 5. Histograms of initial dipole field (D_i) and final dipole field (D_f) for cycles 23 (top panels) and 24 (bottom panels). Lower (-0.11 G) and upper (0.11 G) thresholds are applied in each panel. Data outside these thresholds are combined and shown in the first and last bins.

Figure 6 shows the comparison between D_i and D_f. For some ARs, D_f is larger than D_i, smaller than D_i, or even exhibits a different sign (referred to as changing-sign ARs), as denoted by the red dots. Figure 2 is an example of changing-sign ARs, with D_i of -0.0064 G and D_f of 0.0296 G. The changing-sign ARs are first reported by Jiang et al. (2019). They will be further discussed in Section 4.2. Among ARs with the same sign for D_f and D_i, there are 898 ARs for cycle 23 and 687 ARs for cycle 24 whose axial dipole field decreases (absolute value of D_f smaller than that of D_i). Conversely, there are 403 and 281 ARs for cycles 23 and 24, respectively, whose axial dipole field increases. These changes in dipole fields contribute to the difference between the distributions of D_f and D_i, as illustrated in Figure 5. As the axial dipole fields of most ARs decrease, the distribution of D_f is more concentrated around zero compared to D_i. In both cycles, the number of D_f in bins close to zero surpasses that of D_i. Additionally, as flux transport increases the dipole field of certain ARs, the instances with absolute value greater than 0.1 G for D_f are also more than those for D_i, as shown in Figure 5.

When λ_R is increased from 5° to 7°, the number of ARs with D_f smaller than 0.01G decreases to 1809, accounting for approximately 72.5% of all ARs. In cycles 23 and 24, the number of ARs with dipole field increasing rises from 684 to 991, and for ARs with dipole field decreasing reduces from 1585 to 1374. The contribution of most ARs to the solar dipole field is still small and
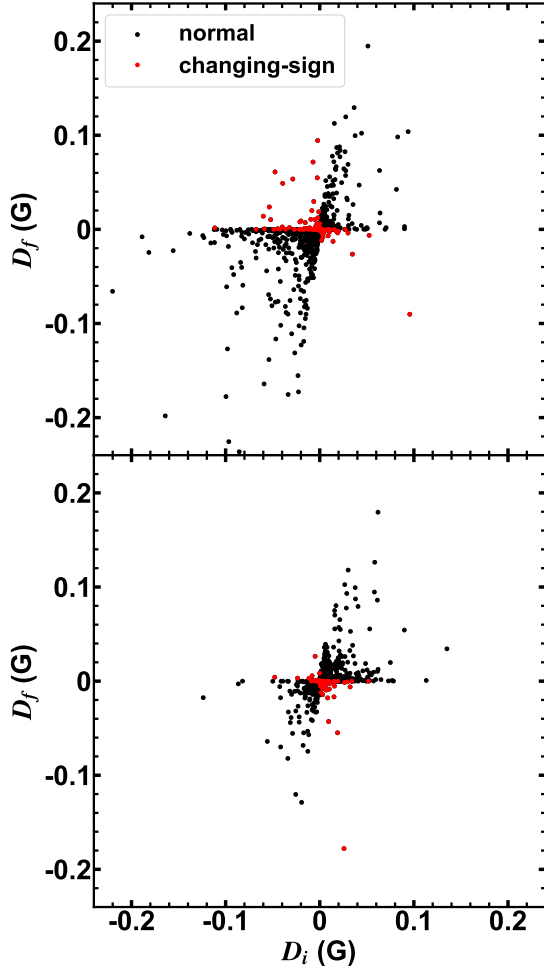
Figure 6. Comparison between the initial dipole field (D_i) and the final dipole field (D_f) of cycles 23 (top panel) and 24 (bottom panel). Data of nine ARs in cycle 23 with absolute D_f larger than 0.24 G are not shown. The black dots label the ARs whose D_i and D_f are of the same sign (normal ARs), and the red dots label the ARs whose D_i and D_f are of different sign (changing-sign ARs). One AR among the nine ARs not shown here changes the sign of the dipole field.

the number of ARs with dipole fields decreasing still exceeds those with dipole fields increasing. The impact of λ_R is limited.

As for the cumulative dipole fields, defined as the sum of all dipole fields, the absolute value of the cumulative final dipole field (cD_f) in each cycle is smaller than that of the cumulative initial dipole field (cD_i). The values of cD_f are -3.91 G for cycle 23 and 1.63 G for cycle 24, while the values of cD_i are -11.85 G for cycle 23 and 4.70 G for cycle 24. However, the cD_f is influenced by the transport parameter λ_R, increasing with λ_R. Consequently, cD_f might surpass cD_i for a larger λ_R. Nevertheless, λ_R is optimized to minimize the de-

viation between cD_f and the solar axial dipole field of each cycle. The dipole field observations of MDI and HMI are -3.88 G and 2.54 G, respectively and the corresponding cD_i values for the MDI and HMI time range are -11.69 G and 3.34 G. These indicate that the absolute values of cD_i are also greater than those of the axial dipole fields of cycles 23 and 24. Therefore, cD_f will consistently be smaller than cD_i as long as λ_R is appropriately chosen. The result is consistent with the finding of cycle 21 by Wang & Sheeley (1991). The fact that the absolute values of cD_f are smaller than that of cD_i indicates that the solar axial dipole field primarily originates from flux emergence. The net effect of flux transport is to reduce the solar dipole field that is obtained during flux emergence. In the jargon of the BL-type mechanism, the generation of the poloidal flux (α-effect) mainly happens in the flux emergence, while the surface flux transport mainly decreases rather than generates the poloidal flux.

4.2. *Impact of the BMR approximation on dipole fields*

The BMR approximation of AR is widely used in AR emergence and evolution research. Here we compare the initial dipole field (D_i) and final dipole field (D_f) calculated using the AR method with those calculated using the BMR method $(D_i^B$ and $D_f^B)$ to test the performance of the BMR approximation. The results are shown in Figure 7. For the initial dipole field, the values of the BMR approximation (D_i^B) are highly consistent with that of the AR method (D_i). This finding is consistent with the research of Yeates (2020). Furthermore, the cumulative initial dipole field of BMR approximation (cD_i^B) and that of AR (cD_i) are also nearly the same. For example, cD_i^B is -11.854 G in cycle 23, while cD_i is -11.850 G. It shows that the BMR approximation of the initial dipole field proposed by Wang & Sheeley (1991) (Equation (4)), is in line with the AR method (Equation (3)). The BMR approximation is more efficient than the AR method and is therefore recommended for use.

However, the real contribution of ARs to the polar field at the solar minimum is D_f, not D_i. For D_f, the BMR approximation yields less satisfactory results. The result aligns with the findings of Wang et al. (2020) but with more data than it. Although the deviations between D_f^B and D_f for many ARs are small, there are instances where the deviations are significant, exceeding 0.1 G, a magnitude comparable to the D_f of these ARs.

Additionally, the BMR approximation sometimes incorrectly predicts the sign of the final dipole field for certain ARs. Given that D_i is nearly equal to D_i^B, and the signs of D_f^B and D_i^B are the same (as seen from
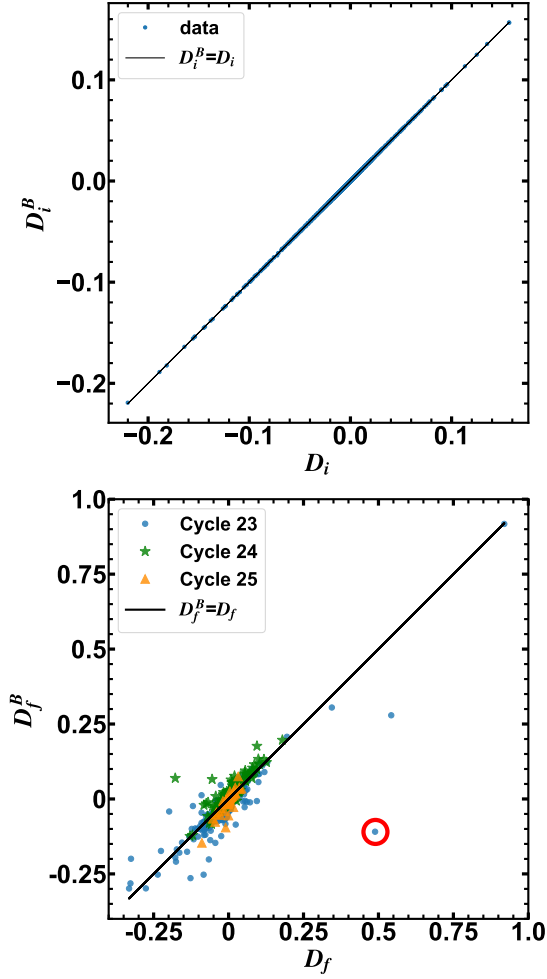
Figure 7. Comparisons between dipole fields. Top panel: the initial dipole field calculated using the AR method (D_i) and the BMR method (D_i^B). Bottom panel: the final dipole field calculated using the AR method (D_f) and the BMR method (D_f^B). The lines in both panels represent the values calculated by the two methods are the same. The red circle in the bottom panel labels an AR with a significant difference between D_f^B and D_f.

Equations (5 - 6)), the sign of D_f^B aligns with D_i. Consequently, ARs with different signs of D_f and D_f^B also exhibit different signs of D_f and D_i. These ARs are referred to as changing-sign ARs in Section 4.1. Among 2952 ARs in cycles 23, 24, and part of 25, there are 266 changing-sign ARs in total. Similarly, Yeates (2020) identifies 53 ARs out of 1090 ARs where D_f obtained with the BMR method and the AR method have different signs. The change in sign is typically attributed to the complex configurations of these ARs, which significantly differ from the BMR model (Jiang et al. 2019). For instance, the AR shown in Figure 2 changes the sign of the dipole field due to the small section of positive po-

larity located at about $-5°$ latitude, which is ignored by BMR approximation. Just like the small positive polarity, these regions emerging near the equator can induce significant variations in both the AR's dipole field and that of the Sun. They should be precisely considered in research, not be approximated.

Some changing-sign ARs have a notable impact on the solar polar field; for example, D_f for the AR labeled with a red circle in Figure 7 is 0.49 G, whereas the BMR approximation D_f^B of it is -0.11 G. The deviation between the BMR approximation and the AR method of the AR is about 0.6 G, about 15% of the total dipole field of cycle 23. To accurately predict the contribution of these changing-sign ARs to the polar field, it is recommended to employ their final dipole field (D_f) while considering their real configurations. The BMR approximation is prone to incorrectly predicting the dipole field of these ARs.

Moreover, the cumulative values of D_f^B and D_f exhibit more significant differences. The cD_f^B and cD_f values are -7.95 G and -3.91 G for cycle 23, and 3.85 G and 1.63 G for cycle 24. The cD_f^B value for each cycle is approximately twice the cD_f value. As the BMR approximation displays a substantial deviation from the AR method, predictions relying on the BMR approximation, as exemplified by Pal & Nandy (2023), may be affected by this deviation, raising concerns about their reliability. For the BMR approximation, D_f^B/D_i^B is proportional to $exp\left(-\frac{\lambda_0^2}{2(\lambda_R^B)^2}\right)$, as shown in Equation (6), where $\lambda_R^B = \sqrt{\frac{\eta}{R_\odot^2 \Delta u} + \sigma_0^2}$. Here, σ_0 represents the initial Gaussian width of the BMR. In our analysis, we take half the polarity separation as σ_0 for the BMR. However, if we set σ_0 as $0°$, the cumulative values of D_f^B become more similar to those of D_f, resulting in -4.39 G for cycle 23 and 2.56 G for cycle 24. The impact of σ_0 on the final dipole field is also discussed by Iijima et al. (2019). The σ_0 of BMRs influences their D_f^B but is challenging to determine accurately. The AR method proposed by Wang et al. (2021) (Equation (8)), which does not require an initial Gaussian width σ_0, can calculate the AR final dipole field more accurately. This shows the advantage of the AR method.

When $\lambda_R = 7°$, the number of changing-sign ARs decreases to 150. The corresponding D_f and D_f^B for the AR labeled in Figure 7 become 0.33 G and -0.08 G, respectively. There is still a large deviation of 0.41 G, approximately 8% of the total dipole field. Significant deviation persists between cD_f^B and cD_f. For instance, cD_f for cycle 23 is -8.05 G, while cD_f^B is -11.12 G. Adjusting the initial Gaussian width σ_0 to 0 improves the BMR approximation, yielding cD_f^B of -8.55 G, closer

to cD_f. When $\lambda_R = 7°$, although the changing-sign ARs are relatively strongly influenced, other results only weakly change. The BMR approximation remains poor for the final dipole field, and setting σ_0 to 0 works better than employing half the polarity separation.

In summary, although the BMR approximation performs well for the initial dipole field, it yields inferior results for the final dipole field, which describes the true contribution of an AR to the polar field in the solar minimum. When measuring an AR's contribution to the polar field, its final dipole field should be utilized while taking into account its real configuration, i.e., the parameter D_f in our database.

4.3. Impact of ARs with small D_f on the cumulative final dipole field
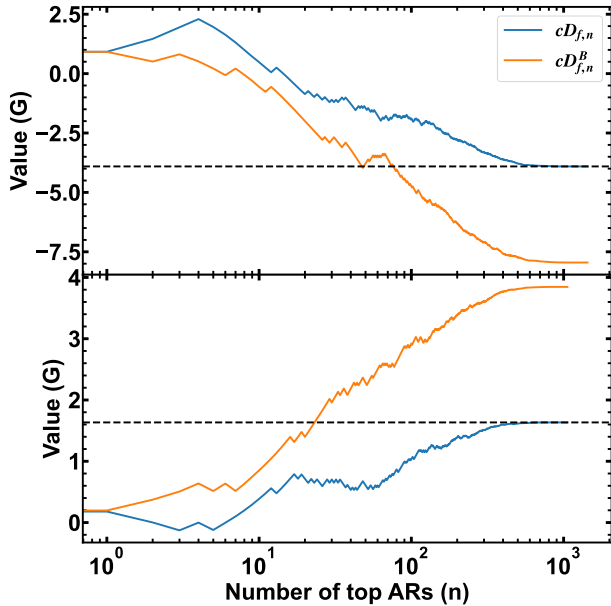
Figure 8. Variation of the cumulative final dipole field for different numbers of top ARs ($cD_{f,n}$, $cD_{f,n}^B$). ARs are ranked by the absolute value of their final dipole field. Both $cD_{f,n}$ for the AR method (blue line) and $cD_{f,n}^B$ for the BMR method (orange line) are shown. The top panel is the result of cycle 23 and the bottom panel is for cycle 24. The black dashed lines in two panels represent the cumulative final dipole fields of all ARs (cD_f) in each cycle.

As shown in Section 4.1, the D_f of most ARs are small. To research the impact of numerous ARs with small D_f, we rank ARs according to the absolute values of their D_f and calculate the cumulative final dipole field for different numbers of top ARs ($cD_{f,n}$). The analysis is conducted with the AR method ($cD_{f,n}$) and the BMR method ($cD_{f,n}^B$). The variations of $cD_{f,n}$ and $cD_{f,n}^B$ with the number of ARs (n) are presented in Figure 8. For

$cD_{f,n}$ calculated with the AR method, its deviation with the cumulative final dipole field of all ARs (cD_f) in each cycle firstly increases due to certain rogue ARs with contributions opposite to those of other ARs. Then, the deviation gradually decreases under the effect of plenty of ARs with small D_f. When the AR number increases to about 500, the $cD_{f,n}$ of two cycles both becomes almost equal to the cD_f. The deviations are 3.3% for cycle 23 and 1.2% for cycle 24. If a similar deviation threshold is set for cycle 24, the AR number decreases to about 350, roughly one-third of all ARs (1059). The 500 ARs also constitute about one-third of all ARs in cycle 23, during which the total number of ARs is 1436. The smallest absolute values of D_f in the top one-third ARs are 0.0028 G and 0.0023 G for cycles 23 and 24, respectively.

For $cD_{f,n}^B$ calculated with the BMR method, the orange line in Figure 8, its deviations with the cumulative final dipole field for all BMRs, cD_f^B, gradually decreases for each cycle with the increase of BMR number without the initial increase for the deviation between $cD_{f,n}$ and cD_f. It shows that these ARs with opposite contributions, which cause the initial increase for the deviation between $cD_{f,n}$ and cD_f, are largely a result of their complex configurations that significantly differ from the BMR. As the number of BMRs increases to around 500, the $cD_{f,n}^B$ values for cycles 23 and 24 also become nearly equivalent to the cD_f^B.

When $\lambda_R = 7°$, the initial increase in the variation of deviation between $cD_{f,n}$ and cD_f with the number of ARs (n) disappears in cycle 24 but persists in cycle 23. This further supports the presence of rogue ARs in cycle 23. The deviations between $cD_{f,n}$ of the top 500 ARs and cD_f are 5.1% and 3% for cycles 23 and 24, respectively. When applying the top 350 ARs, the top one-third ARs of cycle 24, the deviation for cycle 24 is 8%. Although these values are larger than those for $\lambda_R = 5°$, they are still deemed acceptable. The top 500 ARs, or the top one-third ARs, remain sufficient for reconstructing the axial dipole fields during the solar minimum. As for $cD_{f,n}^B$, there is no significant change.

Our results align with the findings of Nagy et al. (2020) and Whitbread et al. (2018), but our study requires a smaller number of ARs, approximately 500 ARs compared to their 750 ARs. These studies reveal that while several rogue ARs can induce noticeable variations in the solar polar field, the collective impact of numerous ARs with smaller contributions to the polar field cannot be disregarded. Notably, not all ARs are essential, and approximately the top 500 ARs, or the top one-third of all ARs, are sufficient for building up the polar field during the solar minimum. Hofer et al. (2024) also em-

phasizes the importance of small ARs on the polar field variation.

5. CONCLUSION AND DISCUSSION

In this paper, we have provided AR parameters including the initial dipole field (D_i), the final dipole field (D_f), and the Bipolar Magnetic Region (BMR) approximations for both parameters, denoted as D_i^B and D_f^B. These AR parameters are part of our live homogeneous database of solar ARs since 1996 and are relevant to solar cycle variability, aiming to improve our understanding and prediction of solar cycles. The properties of these parameters have also been investigated.

Since some ARs can live for many CRs and significantly impact the end-of-cycle polar field, we first introduce a repeat-AR-removal module to identify and remove the repeat detections in our database. This module is not only capable of removing obvious repeat ARs but can also address cases of repeat decayed ARs within activity complexes (ACs). Then we optimize the transport parameter λ_R because it significantly affects the final dipole field, but is poorly constrained by observations. We compare the cumulative final dipole field (cD_f) obtained with different λ_R values and the solar dipole fields derived from the MDI and HMI synoptic magnetograms. It reveals that the optimal λ_R to minimize the deviation between cD_f and solar dipole field is $5°$.

Following the removal of repeat ARs and the optimization of λ_R, we calculate the dipole fields and update the time range of our AR database. Our database now comprises 2892 ARs spanning from CR 1909 to CR 2278 (1996.5 - 2023.11). The database and associated codes are freely available to everyone on GitHub[1] and version 2.0 is archived in Zenodo (Wang et al. 2024). In exploring the properties of the dipole fields, we analyze the distinctions between D_i and D_f, assess the impact of BMR approximation on the dipole field, and evaluate the influence of ARs with small D_f.

The analysis reveals that D_f of an individual AR may be smaller, larger, or even with a different sign compared to its corresponding D_i. However, the cumulative final dipole field (cD_f) of all ARs during a cycle is notably smaller than cD_i for cycles 23 and 24. It aligns with the findings for cycle 21 as reported by Wang & Sheeley (1991). The cumulative final dipole field cD_f smaller than cD_i suggests that flux emergence is the primary source of the solar axial dipole field in the BL

mechanism, and the net effect of flux transport is to decrease the solar dipole field initially obtained during flux emergence. Hence the surface flux transport must be also considered properly to obtain a realistic BL dynamo (Cameron et al. 2012; Jiang et al. 2013; Zhang & Jiang 2022). It is noticeable that the conclusion is based on data from three cycles, and further validation with data from more cycles would enhance its robustness.

While the BMR approximation works well for D_i, it exhibits poor performance for D_f. The deviation between the BMR approximation and real ARs is even more pronounced for cD_f. Specifically, for ARs that change the sign of their dipole fields during flux transport, the BMR approximation fails to predict the sign of their D_f. It introduces a considerable deviation compared to D_f without approximation. Therefore, it is advisable to utilize the final dipole field while taking into account the real configuration of ARs, i.e. D_f in our database, to measure an AR's contribution to the polar field accurately.

While the impact of most ARs is limited, their effects can not be ignored. About the top 500 ARs, ordered by their absolute D_f, are necessary to build up the polar field in the solar minimum. This result is consistent with the results of Whitbread et al. (2018) and Nagy et al. (2020).

In optimizing transport parameter λ_R, the deviation between cD_f and solar dipole field for the optimal λ_R still can not be ignored, suggesting that $5°$ may not be so perfect. The deviation may be caused by the detection of new ARs in the ACs, limitations in synoptic magnetogram observations, and limitations in polar field observations. The deviation may also be caused by the possible variation of transport parameter λ_R with solar cycles (Wang et al. 2009; Whitbread et al. 2017). To assess the impact of λ_R on the presented results, we also provide the results for $\lambda_R = 7°$. These results indicate that while λ_R significantly influences D_f, the distinctions between D_i and D_f, the impact of BMR approximation on D_f, and the influence of ARs with small D_f are only weakly affected by λ_R.

This is the second paper of a series that aims to construct a live, comprehensive, and homogeneous AR database. In the first paper of the series (Wang et al. 2023), we identified all ARs based on the MDI and HMI synoptic magnetograms and provided some fundamental parameters as the first set of parameters. In this paper, we provide the dipole fields as the second set of parameters. In the future, we will continue to provide more parameters and deeply analyze AR properties, particularly those of rogue ARs. An important parameter to be explored is the Degree of Rogueness (DoR). Nagy et al.

---

[1] AR database: https://github.com/Wang-Ruihui/A-live-homogeneous-database-of-solar-active-regions/tree/with-repeat-AR-Removal-and-params-dipole-fields.

(2020) suggests that only about the top 10-50 DoRs are required to build up the polar field in solar minimum, while the other ARs could be simplified. Their results significantly reduce the number of ARs necessary and show the importance of the DoR. However, based on our database, we find DoR is affected by the statistical result applied in its calculation, and the result of the top 50 DoRs while simplifying the other ARs may be not so ideal as shown by Nagy et al. (2020). Further exploration and discussion on the DoR are planned for future work.

REFERENCES

Babcock, H. W. 1961, ApJ, 133, 572, doi: 10.1086/147060

Bobra, M. G., Sun, X., Hoeksema, J. T., et al. 2014, SoPh, 289, 3549, doi: 10.1007/s11207-014-0529-3

Bobra, M. G., Wright, P. J., Sun, X., & Turmon, M. J. 2021, ApJS, 256, 26, doi: 10.3847/1538-4365/ac1f1d

Cameron, R. H., Dasi-Espuig, M., Jiang, J., et al. 2013, A&A, 557, A141, doi: 10.1051/0004-6361/201321981

Cameron, R. H., Schmitt, D., Jiang, J., & Işık, E. 2012, A&A, 542, A127, doi: 10.1051/0004-6361/201218906

Cheung, M. C. M., Rempel, M., Title, A. M., & Schüssler, M. 2010, ApJ, 720, 233, doi: 10.1088/0004-637X/720/1/233

Fan, Y. 2009, Living Reviews in Solar Physics, 6, 4, doi: 10.12942/lrsp-2009-4

Gaizauskas, V., Harvey, K. L., Harvey, J. W., & Zwaan, C. 1983, ApJ, 265, 1056, doi: 10.1086/160747

Harvey, K. L. 1993, PhD thesis, -

Hofer, B., Krivova, N. A., Cameron, R., Solanki, S. K., & Jiang, J. 2024, A&A, 683, A48, doi: 10.1051/0004-6361/202245635

Iijima, H., Hotta, H., & Imada, S. 2019, ApJ, 883, 24, doi: 10.3847/1538-4357/ab3b04

Jiang, J., Cameron, R. H., Schmitt, D., & Işık, E. 2013, A&A, 553, A128, doi: 10.1051/0004-6361/201321145

Jiang, J., Cameron, R. H., & Schüssler, M. 2014a, ApJ, 791, 5, doi: 10.1088/0004-637X/791/1/5

—. 2015, ApJL, 808, L28, doi: 10.1088/2041-8205/808/1/L28

Jiang, J., Chatterjee, P., & Choudhuri, A. R. 2007, MNRAS, 381, 1527, doi: 10.1111/j.1365-2966.2007.12267.x

Jiang, J., Hathaway, D. H., Cameron, R. H., et al. 2014b, SSRv, 186, 491, doi: 10.1007/s11214-014-0083-1

Jiang, J., Song, Q., Wang, J.-X., & Baranyi, T. 2019, ApJ, 871, 16, doi: 10.3847/1538-4357/aaf64a

Jiang, J., Wang, J.-X., Jiao, Q.-R., & Cao, J.-B. 2018, ApJ, 863, 159, doi: 10.3847/1538-4357/aad197

Jiang, J., Zhang, Z., & Petrovay, K. 2023, Journal of Atmospheric and Solar-Terrestrial Physics, 243, 106018, doi: 10.1016/j.jastp.2023.106018

Leighton, R. B. 1964, ApJ, 140, 1547, doi: 10.1086/148058

Lemerle, A., Charbonneau, P., & Carignan-Dugas, A. 2015, ApJ, 810, 78, doi: 10.1088/0004-637X/810/1/7810. 48550/arXiv.1511.08548

Li, Y., & Welsch, B. T. 2008, in Astronomical Society of the Pacific Conference Series, Vol. 383, Subsurface and Atmospheric Influences on Solar Activity, ed. R. Howe, R. W. Komm, K. S. Balasubramaniam, & G. J. D. Petrie, 397

Luo, Y., Jiang, J., & Wang, R. 2023, ApJ, 954, 199, doi: 10.3847/1538-4357/acec77

Muñoz-Jaramillo, A., Dasi-Espuig, M., Balmaceda, L. A., & DeLuca, E. E. 2013, ApJL, 767, L25, doi: 10.1088/2041-8205/767/2/L25

Muñoz-Jaramillo, A., Navarrete, B., & Campusano, L. E. 2021, ApJ, 920, 31, doi: 10.3847/1538-4357/ac133b

Nagy, M., Lemerle, A., Labonville, F., Petrovay, K., & Charbonneau, P. 2017, SoPh, 292, 167, doi: 10.1007/s11207-017-1194-0

Nagy, M., Petrovay, K., Lemerle, A., & Charbonneau, P. 2020, Journal of Space Weather and Space Climate, 10, 46, doi: 10.1051/swsc/2020051

Pal, S., & Nandy, D. 2023, arXiv e-prints, arXiv:2312.15703, doi: 10.48550/arXiv.2312.15703

Petrovay, K. 2020, Living Reviews in Solar Physics, 17, 2, doi: 10.1007/s41116-020-0022-z

Petrovay, K., Nagy, M., & Yeates, A. R. 2020, Journal of Space Weather and Space Climate, 10, 50, doi: 10.1051/swsc/2020050

Schatten, K. H., Scherrer, P. H., Svalgaard, L., & Wilcox, J. M. 1978, Geophys. Res. Lett., 5, 411, doi: 10.1029/GL005i005p00411

Scherrer, P. H., Bogart, R. S., Bush, R. I., et al. 1995, SoPh, 162, 129, doi: 10.1007/BF00733429

Scherrer, P. H., Schou, J., Bush, R. I., et al. 2012, SoPh, 275, 207, doi: 10.1007/s11207-011-9834-2

Sreedevi, A., Jha, B. K., Karak, B. B., & Banerjee, D. 2023, ApJS, 268, 58, doi: 10.3847/1538-4365/acec47

Sun, X. 2018, arXiv e-prints, arXiv:1801.04265, doi: 10.48550/arXiv.1801.04265

Sun, X., Liu, Y., Hoeksema, J. T., Hayashi, K., & Zhao, X. 2011, SoPh, 270, 9, doi: 10.1007/s11207-011-9751-4

Tlatov, A. G., Vasil'eva, V. V., Makarova, V. V., & Otkidychev, P. A. 2014, SoPh, 289, 1403, doi: 10.1007/s11207-013-0404-7

van Ballegooijen, A. A., Cartledge, N. P., & Priest, E. R. 1998, ApJ, 501, 866, doi: 10.1086/305823

van Driel-Gesztelyi, L., & Green, L. M. 2015, Living Reviews in Solar Physics, 12, 1, doi: 10.1007/lrsp-2015-1

van Driel-Gesztelyi, L., & Petrovay, K. 1990, SoPh, 126, 285, doi: 10.1007/BF00153051

Wang, R., Jiang, J., & Luo, Y. 2023, ApJS, 268, 55, doi: 10.3847/1538-4365/acef1b

Wang, R., Jiang, J., & Luo, Y. 2024, A live homogeneous database of solar active regions with repeat ARs removal and parameters for solar cycle variability, v2.0, Zenodo, doi: 10.5281/zenodo.11115058

Wang, Y. M. 2017, SSRv, 210, 351, doi: 10.1007/s11214-016-0257-0

Wang, Y. M., Robbrecht, E., & Sheeley, N. R., J. 2009, ApJ, 707, 1372, doi: 10.1088/0004-637X/707/2/1372

Wang, Y. M., & Sheeley, N. R., J. 1989, SoPh, 124, 81, doi: 10.1007/BF00146521

—. 1991, ApJ, 375, 761, doi: 10.1086/170240

Wang, Z.-F., Jiang, J., & Wang, J.-X. 2021, A&A, 650, A87, doi: 10.1051/0004-6361/202140407

Wang, Z.-F., Jiang, J., Zhang, J., & Wang, J.-X. 2020, ApJ, 904, 62, doi: 10.3847/1538-4357/abbc1e

Whitbread, T., Yeates, A. R., & Muñoz-Jaramillo, A. 2018, ApJ, 863, 116, doi: 10.3847/1538-4357/aad17e

Whitbread, T., Yeates, A. R., Muñoz-Jaramillo, A., & Petrie, G. J. D. 2017, A&A, 607, A76, doi: 10.1051/0004-6361/201730689

Yeates, A. R. 2020, SoPh, 295, 119, doi: 10.1007/s11207-020-01688-y

Yeates, A. R., Cheung, M. C. M., Jiang, J., Petrovay, K., & Wang, Y.-M. 2023, SSRv, 219, 31, doi: 10.1007/s11214-023-00978-8

Zhang, Z., & Jiang, J. 2022, ApJ, 930, 30, doi: 10.3847/1538-4357/ac6177